UNIVERSITY OF CALIFORNIA,
IRVINE

Vapor Chamber External and Internal Factors Investigation

DISSERTATION

submitted in partial satisfaction of the requirements
for the degree of

MASTER OF SCIENCE

in Mechanical and Aerospace Enginnering

by

Bowen Liu

Dissertation Committee:
Professor Yoonjin Won, Chair
Professor Yun Wang
Professor Penghui Cao

2020

DEDICATION

To my family.

TABLE OF CONTENTS

LIST OF FIGURES

LIST OF TABLES

ACKNOWLEDGMENTS

I would like to thank my advisor, professor Yoonjin Won for giving me advice and opportunity to conduct experiments.
I would like to thank my friend Pengjie Tian and Dongyang Li for supporting me.
I would like to thank Chenghui Lin, Quang Phan for teaching me how to build experiment setup and think as a researcher.

ABSTRACT OF THE DISSERTATION

Vapor Chamber External and Internal Factors Investigation

By

Bowen Liu

Master of Science in Mechanical and Aerospace Enginnering

University of California, Irvine, 2020

Professor Yoonjin Won, Chair

The increasing power density of smartphone chipset urges the demand of high-heat-flux removal techniques. Conventionally, smartphone manufacturers used aluminum, copper, and graphene sheet to spread the heat generated by the chipset. However, the specific heat capacity of those material limits the chip power dissipation. A vapor chamber, which takes advantage of the specific heat capacity and the latent heat of fluid, can increase the limit of the chipset power dissipation. This work performs experimental and computational studies to investigate factors that affect the vapor chamber thermal conductivity. It has been found that the vapor chamber can be affected by gravity, the porosity of the porous media, the pore size of the porous media, surface energy of the internal structure, and boundary conditions. Gravity helps the liquid phase flow back to the evaporator. The porosity and pore size of the porous media can enhance the capillary pressure and postpone the boiling nucleation. The surface energy of the internal structure can force the nucleation sites in the evaporator section. The understanding of these factors can pave a way for designing a vapor chamber.

Chapter 1

Introduction

Nowadays, a smart-phone chipset has increased its frequency and power delivery dramatically, while the size of the chipset is being miniaturized. One reason for increasing power is based on the Moore's law, which stated that the number of transistors inside a chip could be double about 18 months, as shown in figure 1.1 (a) [10]. Another reason is that the multicore architectures had further increased the heat generation by the chipset [20]. As shown in figure 1.1 (b), since 2010, the CPU power density had exceeded 100W/cm^2 [9]. Such a high power density of the chipset can cause electronic devices running at high temperature, which can lead to thermal expansion mismatch, thermal fracture, reduce the lifetime of the electronic devices, and the failure of the electronic devices. Such high power density also means that heat can be cumulated at one spot, which is identified as a hot spot. A hot spot can cause thermal pain to smartphone users [32]. Generally, air cooling with a heat sink and a fan and metal heat spreader are the main strategies [16]. However, air cooling with a fan is an active cooling method and requires additional power consumption, which lowers the battery life. The metal heat spreader can not prevent the hot spot.

A promising thermal management method is a phase change heat transfer device, such as a

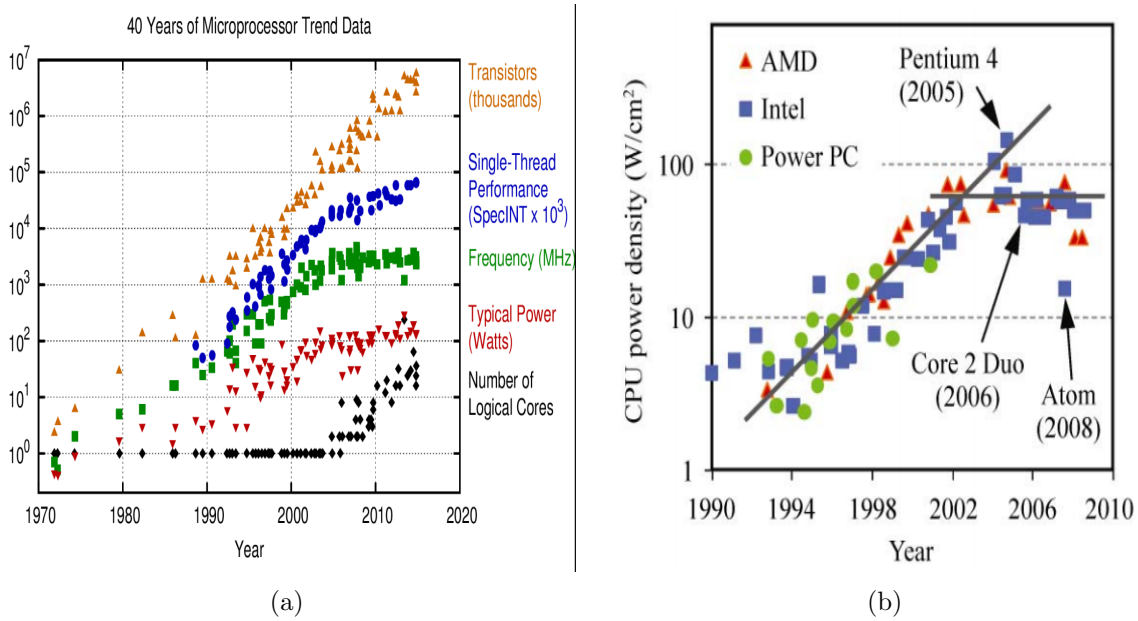

(a) (b)

Figure 1.1(a) Moore's law and recent data [28], and (b) CPU power density as a function of time [9]. It showed that the power density of electronic device increased with time becuase the number of transistors inside the chip increases with the time.

vapor chamber. A vapor chamber, as a great passive heat spreader, has high thermal conductivity, and is a good candidate to solve the hot spot issue. It has three major components: a working fluid, wick structure, and vapor channel [6]. Shahed et al. reported a copper-based center fiber wick vapor chamber with thermal conductivity 2300 W/MK [1]. Oshman et al. fabricated a polymer-based vapor chamber with thermal conductivity 830 W/MK [8]. Lewis et al. manufactured a copper 200 and nylon-based vapor chamber with thermal conductivity 1533 W/MK [29]. The thermal conductivity of the vapor chambers showed 2-4 times higher than that of the natural metal. However, those vapor chambers have large sizes, which is impossible to fit in a smartphone. For instance, the Samsung S7 has a vapor chamber, which has a dimension of 0.4 mm thick, 77.28 mm long, and 2.91 mm wide by experimental measurement. Shahed et al. also reported that the thinner vapor chamber reduced its thermal conductivity [1]. It means that scaling down those vapor chamber designs is not a solution.

Most of the vapor chambers are made of metal. The massive production of the metal vapor chambers could be expensive. Furthermore, the rigidity and high electrical conductivity of

the metal cause that the metal vapor chambers are not suitable to remove the hot spot of high sensitivity electronic device [30]. Therefore, the polymer vapor chamber could be an alternative option, where the polymer has low electrical conductivity and high-chemical reaction resistance [7]. Since the polymer has low thermal conductivity, a vapor chamber design made by polymer has lower thermal conductivity than the same vapor chamber design made by metal. However, the thermal conductivity of non-metal porous media can be increased with the two phase-flow. Wang et al. found that the thermal conductivity of carbon paper could be enhanced as the paper is saturated with liquid water[43]. Therefore, it is necessary to study which factor can affect the thermal conductivity of the vapor chamber and to find a possible design for a polymer vapor chamber design. In this work, both experimental and computational studies are performed to investigate the factor effects.

1.1 Background

A vapor chamber has three major components, as shown in figure 1.2. Typically, the wick structure, on the heat source side, is designed to be hydrophilic. The wick structure, on the condenser side, is designed to be hydrophobic [29]. The heat source is attached to the evaporator side of the vapor chamber. The liquid at the evaporator side will absorb the latent heat and evaporate to vapor. The vapor will rise to the top condenser and condensate to liquid droplets. The liquid droplet, under the gravity force and capillary pressure, will drop back to the bottom wick and move toward the evaporator through the capillary wick structure. Therefore, inside the vapor chamber, it is a two-phase fluid dynamic system. To improve the thermal conductivity of the vapor chamber is to facilitate the evaporation and condensation process. For instance, Wang et al. found that a two-phase flow system works without degradation, as it maintained the ration between the rate of water addition over the rate of water removal via diffusion and evaporation is close to one [42, 41]. This ratio could

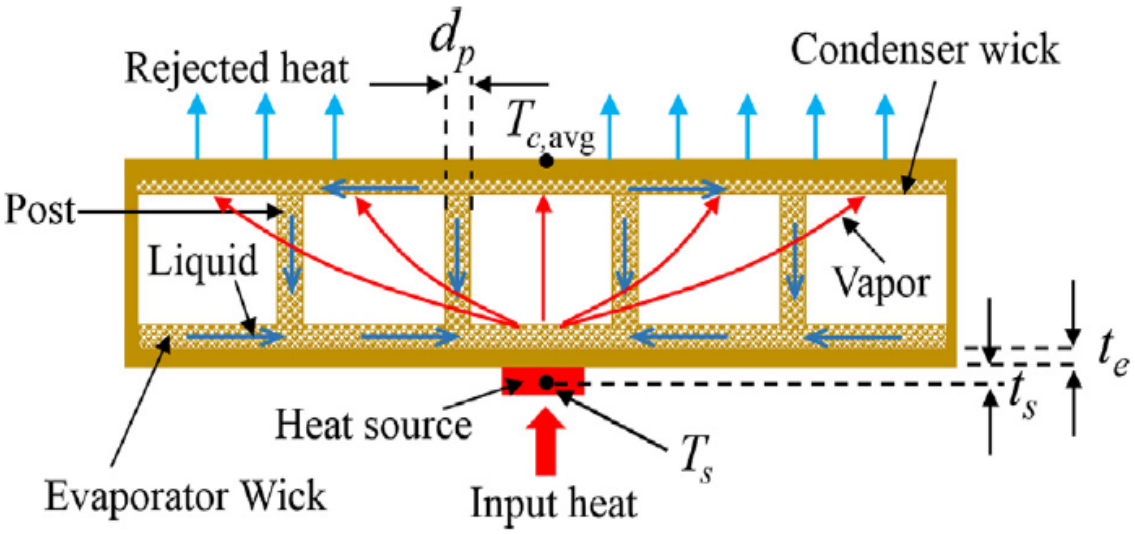

Figure 1.2 Vapor chamber schematic: the vapor chamber is composed of heat source, evaporator wick, post, and condenser wick. Basically, the liquid at the evaporator side will absorb the latent heat and evaporate to vapor. The vapor will rise to the top condenser and condensate to liquid droplets. The liquid droplet, under the gravity force and capillary pressure, will drop back to the bottom wick and move toward the evaporator through the capillary wick structure.

be used to quantify the two-phase flow performance.

The working principle of a vapor chamber is similar to the working principle of a heat pipe [19, 33]. The difference between the vapor chamber and the heat pipe is the heat conduction method. The heat pipe generally has a heat source at one side so that its conduction method is one-dimension. On the other hand, the vapor chamber has a heat source at the center so that its conduction method is two-dimension, as shown in figure 1.2. Therefore, generally, the vapor chamber has much higher thermal conductivity than the heat pipe.

Since the vapor chamber is a dynamic system, the thermal conductivity of the vapor chamber can vary at different heat power input [17, 23, 39]. The maximum input heat flux that a vapor chamber can transfer is named as the critical heat flux, where several bubble nucleation sites merge to form a vapor film. The vapor film formation also means that the liquid can not be transported back to the evaporation sites. For years, researchers tried to enhance the CHF by changing the morphology inside the vapor chamber. Wong et al. designed parallel

grooves on the inner surface of the top plate to replace a flat top plate [31]. They found that this method could reduce the evaporation and condensation resistance since they increased the liquid-vapor interface. Ji et al. used copper foam as a wick structure and found that the multiscale pore size of the porous media improved the liquid and vapor transportation [37]. Their design helped the vapor release from large pores and liquid suction in small pores. Mete et al. coated copper surface with a perfluoro alcohol-isocyanate polymer solution and decreased the surface energy of the copper [18]. They also improved the thermal conductivity of the vapor chamber because the decreased surface energy made the copper hydrophobic so that the vapor density at the evaporation section could be lower. Conclusively, they facilitated the evaporation process.

1.2 Motivation of Objectives of the Thesis

Since the cost of massive production of the metal vapor chamber could be expensive, the polymer vapor chamber could be an alternative choice, where the polymer material is much cheaper than the metal material. Although the polymer material has poor thermal conductivity, a good vapor chamber design can have thermal conductivity several times higher than the metal material has. Therefore, a polymer vapor chamber could be an alternative solution to prevent the hot spot problem inside a smartphone but few literatures studied the polymer vapor chamber, which can fit inside the smartphone. At the current stage, the polymer vapor chamber design still has much lower thermal conductivity than the metal vapor chamber, due to the poor thermal conductivity of the polymer material and the degradation of wetting, evaporation and condensation process for a small size design.

Therefore, to conquer the dilemma, this work aims at investigating high thermal conductivity polymer material, factors that affect the thermal performance of the vapor chamber, and the two-phase flow transportation inside a vapor chamber. These were achieved by researching

the newest papers that studied the thermal conductivity of the polymer material, experimental studies on the external and internal factors that affected the thermal performance of the vapor chamber, and simulation studies that revealed the liquid-vapor and temperature distribution inside the vapor chamber. Conclusively, factors that should be considered to manufacture a polymer vapor chamber were identified. The polymer material that could be used to manufacture the polymer vapor chamber was also identified.

Chapter 2

Vapor Chamber Parameter Analysis and Analytical Model

2.1 Vapor Chamber Parameter Analysis

To determine the effective thermal conductivity of the vapor chamber, massive factors should be considered [1-15]. They can be divided into two major categories: external and internal factors. External factors include heat source power, heat sink power, and gravity. Internal factors include physical properties of the working fluid, the wick structure, and the dimension of the vapor chamber. All factors affect the effective thermal conductivity but have different weight.

2.1.1 External Factor

According to Fourier's law, the effective thermal conductivity can be calculated based on the following equation:

$$q = \frac{kdT}{dx} \qquad or \qquad k = \frac{qdx}{dT} \tag{2.1}$$

where k is effective thermal conductivity, dT is temperature difference, dx is the distance difference between two measured temperature point, and q is the heat flux.

A vapor chamber, unlike a solid metal conductor, does not have a constant k since it is a passive dynamic system [1-16]. Therefore, the external factors have affected the effective thermal conductivity of the vapor chamber. The heat source power and the heat sink power determine the q and dT/dx. Furthermore, the vapor chamber is also a fluid problem. The gravity should be also considered as an external factor. To summarize it up, the following equation could be written:

$$k_{external} = f(q, \frac{dT}{dx}, g) \tag{2.2}$$

2.1.2 Interal Factor

Inside the vapor chamber, there are fluid and solid parts. Since water is quite stable fluid and has one of the highest heat capacity around 4.22 KJ/KgK, it has been selected as the working fluid [4]. Therefore, the physical properties involved with the working fluid can be assumed as a constant.

As shown in figure 1.2, the solid part of the vapor chamber is composed of evaporator wick, condenser wick, and post structure. The wick structures are porous media, where liquid can be transported. The post structure supports the entire vapor chamber and it also allows

the liquid flow from the condenser to the evaporator. Furthermore, the size of the post determines the size of the cavity for vapor. To design these structure, porosity and pore size should be considered [37, 25]. Singh et al. showed that the capillary pressure can be increased with smaller pore size and high porosity so that the thermal conductivity of the heat pipe can be increased [25].

Vapor film at the evaporator side is the main cause of the vapor chamber overheating. Bubble nucleation sites regulation can postpone the vapor film formation [21]. Through changing the internal structure surface energy, it is possible to limit the bubble nucleation site. Conclusively, the following equation could be driven:

$$k_{internal} = f(\varepsilon, d, \gamma, h, t) \tag{2.3}$$

where ε is the porosity of the wick structure, d is the pore size of the wick structure, γ is the surface energy of the wick structure, h is the height of the post structure, and t is the thickness of the wick structure.

2.2 Analytical Model

2.2.1 Governing Equation

Since liquid-water is dominant at the wick structures, the continuity and momentum equation to describe the liquid-water flow can be written as follows:

conservation equation :

$$\frac{\partial \rho\varepsilon}{\partial t} + \nabla \cdot (\rho \vec{V} u) = 0 \tag{2.4}$$

x-momentum equation :

$$\frac{\partial \rho u}{\partial t} + \nabla \cdot (\rho \vec{V} u) = -\frac{\partial \rho\varepsilon}{\partial x} + \nabla \cdot (\mu \nabla u) - \frac{\mu\varepsilon}{K} u - \frac{C_E \varepsilon}{K^{1/2}} \rho |\vec{V}| u \tag{2.5}$$

y-momentum equation :

$$\frac{\partial \rho v}{\partial t} + \nabla \cdot (\rho \vec{V} v) = -\frac{\partial \rho\varepsilon}{\partial y} + \nabla \cdot (\mu \nabla u) - \frac{\mu\varepsilon}{K} v - \frac{C_E \varepsilon}{K^{1/2}} \rho |\vec{V}| v \tag{2.6}$$

z-momentum equation :

$$\frac{\partial \rho w}{\partial t} + \nabla \cdot (\rho \vec{V} w) = -\frac{\partial \rho\varepsilon}{\partial z} + \nabla \cdot (\mu \nabla w) - \frac{\mu\varepsilon}{K} w - \frac{C_E \varepsilon}{K^{1/2}} \rho |\vec{V}| w \tag{2.7}$$

where ρ is the water-liquid and water-vapor density at wick stucture and vapor cavity respectively, ε is the porosity, K is the permeability, μ is the dynamic viscosity of water, and C_E is the Ergun's coefficient 0.55. The energy equation in the wall, wick and vapor core can be written as follows:

$$\frac{(\rho C)_m T}{t} + \nabla \cdot [\rho C \vec{V} T] = \nabla \cdot (k_{eff} \nabla T) \tag{2.8}$$

$$At \quad Wall \ (\rho C)_m = (\rho C)_s \tag{2.9}$$

$$At \quad Wick : (\rho C)_m = (1-\varepsilon)(\rho C)_s + \varepsilon (\rho C)_l \tag{2.10}$$

$$At \quad Vapor \quad Cavity : (\rho C)_m = (\rho C)_v \tag{2.11}$$

where C is the specifc heat and K_eff is the thermal conductivity of the solid material.

The phase change equation is based on Lee's model, which can be written as following:

$$\dot{m_{fg}} = r_i \alpha_f \rho_f \frac{T_f - T_{sat}}{T_{sat}} \quad for \quad evaporation(T_f > T_s at) \tag{2.12}$$

$$\dot{m_{gf}} = r_i \alpha_g \rho_g \frac{T_{sat} - T_g}{T_{sat}} \quad for \quad evaporation(T_g < T_s at) \tag{2.13}$$

where α_f and α_g are liquid volume fraction and vapor volume fraction respectively, and r_i is mass transfer intesity factor, which is an emperical number. Here, r_i for evaporation and condensation constant is 0.2 and 0.25 respectively.

Additional detail mathmatical derivation can be found in [26, 35, 24, 11].

2.2.2 2-D Numerical Method

The aforementioned governing equations describe the vapor chamber. However, it is hard to solve them analytically. Therefore, a numerical method is applied here. First, the thickness and the length of the vapor chamber are t and l. These terms determine the mesh size of the numerical solution along x and y direction. The mesh node can be written as follwoing:

$$N_x = \frac{l}{\delta x} \tag{2.14}$$

$$N_y = \frac{t}{\delta y} \tag{2.15}$$

where N_x is the number of nodes along x, and N_y is the numer of nodes along y. In this work, $\delta x = \delta y = 3e^{-4}$. Therefore, the mesh is uniform distributed. In total, there are 7610 nodes.

Then the uniform grid size is used to discretize the governing equation from the PDE equation to algebraic equations. Then equation can be written as:

conservation equation :

$$\sum_i (\rho U \cdot \hat{n_i} \cdot u \cdot \Delta S_i)_{face} = 0 \tag{2.16}$$

x-direction momentum:

$$\sum_i (\rho U \cdot \hat{n_i} \cdot u \cdot \Delta S_i)_{face} = (-\frac{\bar{\partial} p}{\partial x} \cdot \Delta V)_{cell} + \mu \cdot \sum_i (\nabla u \cdot \hat{n_i} \cdot \Delta S_i)_{face} + f_x \tag{2.17}$$

$$f_x = ((-\frac{\mu \varepsilon}{K} u - \frac{C_E \varepsilon}{K^{1/2}} \rho |\vec{V}| u) \cdot \Delta V)_{cell} \tag{2.18}$$

y-direction momentum:

$$\sum_i (\rho U \cdot \hat{n_i} \cdot v \cdot \Delta S_i)_{face} = (-\frac{\bar{\partial} p}{\partial y} \cdot \Delta V)_{cell} + \mu \cdot \sum_i (\nabla v \cdot \hat{n_i} \cdot \Delta S_i)_{face} + f_y \tag{2.19}$$

$$f_y = ((-\frac{\mu \varepsilon}{K} v - \frac{C_E \varepsilon}{K^{1/2}} \rho |\vec{V}| v) \cdot \Delta V)_{cell} \tag{2.20}$$

where $\rho U \cdot \hat{n_i} \cdot u \cdot \Delta S_i$ is the mass flux through a cell, ΔS_i is the area of the cell, n_i is the normal vector of the faces, and ΔV is the volume of the cell. Here, since the model is 2-D, Z-momentum equation is neglected.

The boundary condition gives as follows:

condensation section (top wall):

$$-k_w \frac{\partial T}{\partial y} = h_c (T - T_c) \tag{2.21}$$

evaporation section (bottom wall):

$$k_w \frac{\partial T}{\partial y} = q_e \tag{2.22}$$

lateral wall:

$$-k_w \frac{\partial T}{\partial y} = h_c(T - T_c) \tag{2.23}$$

Furthermore, the intial condition gives as follows:

$$T(x, y, 0) = T_{roomtemperature} \tag{2.24}$$

$$P_{initial} = P_{sat}(T_b oiling) \tag{2.25}$$

Based on the intial and boundary condition, equation 2.16 to 2.30 could be written in a matrix form, as follwoing:

$$Ax = b \tag{2.26}$$

where A is the coefficient of the pressure terms, x is$\frac{\partial P}{\partial x}$ and $\frac{\partial P}{\partial y}$, and b is the summation of other terms including boundary condition and intial condition. Then a tridiagonal matrix could be otained to sovle. The aforemetioned method is solved in the Ansys fluent in pressure-based model. Additional detail of the Ansys finite volume method could be found in [12].

Further to make sure the model is correct, the pressure-based solution follows the convergence criteria, as shown in figure 2.1. It means that the model is correct as if the model is converged. However, it could be unrealistic. The detail analysis and result could be found in chapter 4.

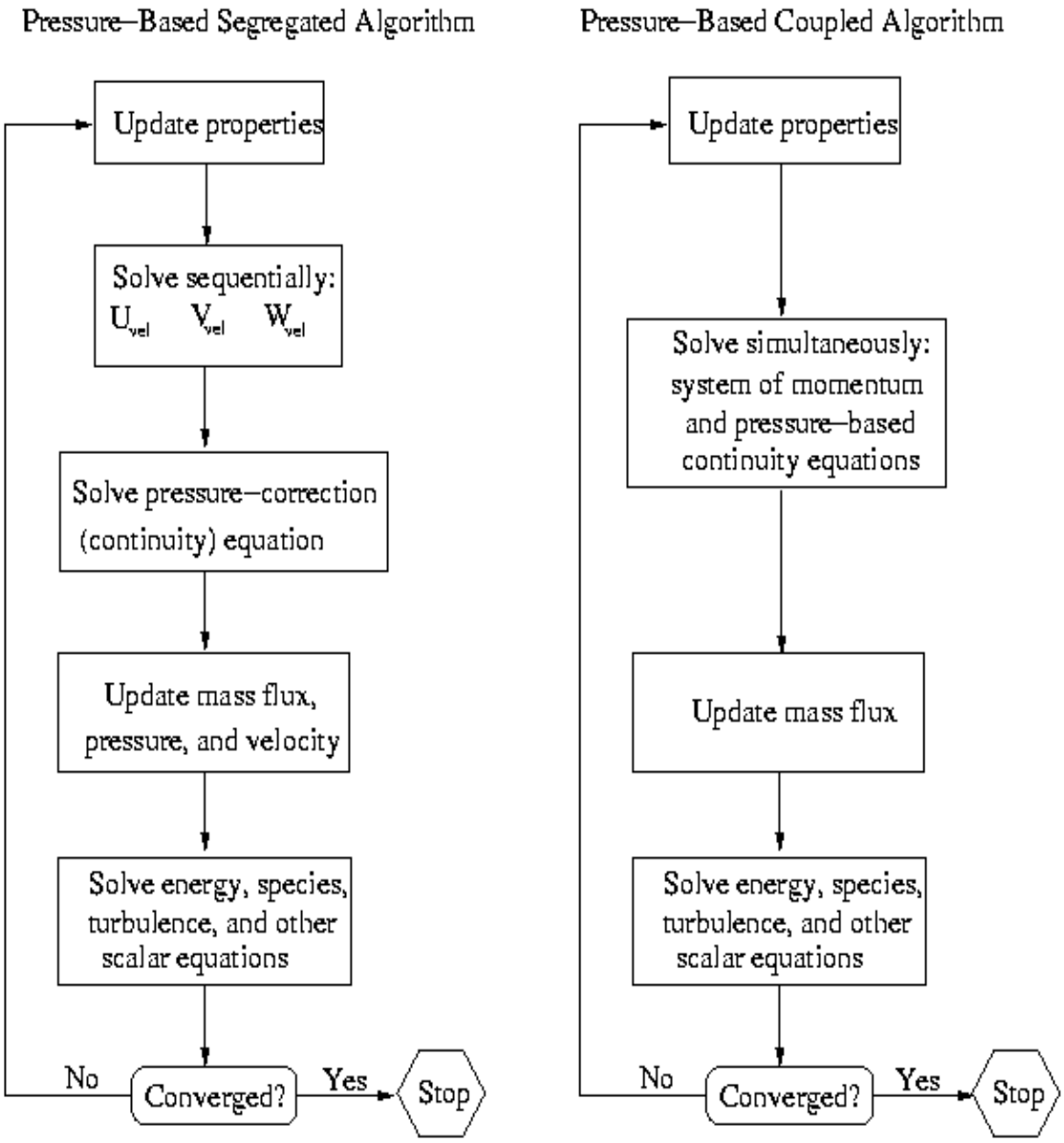

Figure 2.1 Overview of the pressure based solution methods[3]. The Ansys software takes the input value including boundary and initial condition into the aforementioned equations, and compares the calculated result with the inital result. As the residual is less than a certain number, the ansys will print the result.

Chapter 3

External Factor Experiment Setup and Result

3.1 External Factor Experiment

3.1.1 External Factor Experiment Setup

To study the external factor effects on the vapor chamber or heat pipe thermal conductivity, an experimental setup is designed, as shown in figure 3.1.

The cartridge heater is inserted inside an aluminum block. As a voltage applies to the cartridge heater, the heater can generate heat, which is transported through the aluminum block. Two thermocouples are placed on the block and take the temperature reading (T_1

and T_2). Based on Fourier's law, the heat flux generated by the heater can be calculated:

$$q_{in} = \frac{T_2 - T_1}{k_{Al} dx_{Al}} \tag{3.1}$$

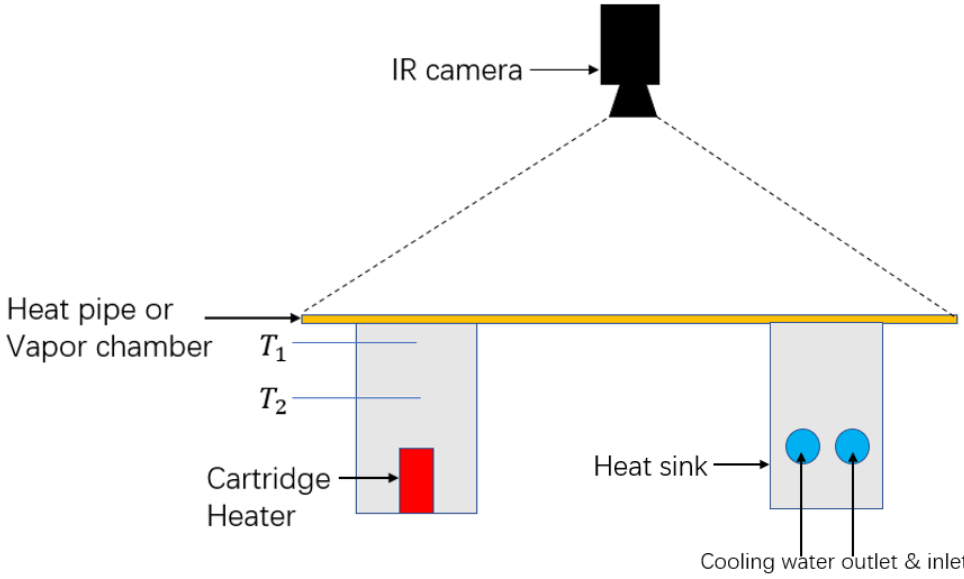

Figure 3.1 Vapor chamber experiment set up. The cartridge heat is not directly used as the heat source because the uniform heat flux is expected to apply to the heat pipe test. The heat sink is used to avoid overheating the heat pipe samples. The IR camer is used to record the temperature profile. T_1 and T_2 is used to calculate the uniform heat flux.

where k_{Al} is the effective thermal conductivity of aluminum, dx_{Al} is the distance between two measured temperature point, and $q_{in}$is the heat flux generated by the cartridge heater.

IR camera, which can provide high accuracy and a surface temperature reading, is used to record the steady-state temperature profile. Three IR image results are shown in figure 3.2 The effective thermal conductivity, thus, can be approximated by taking multiple points on

the IR images and using Fourier's law to get an average thermal conductivity.

$$k_{vc} = \frac{1}{N} \sum_{i=1}^{i=N} \frac{(dT)_N}{q dx_{vc}} \tag{3.2}$$

Table 3.1
Dimension of the heat pipes.

sample	*Length*(*mm*)	*Thicknes*(*mm*)	*Width*(*mm*)
S7	77.28	0.40	2.91
S8	85.66	0.41	2.92
S1	61.62	0.40	8.93

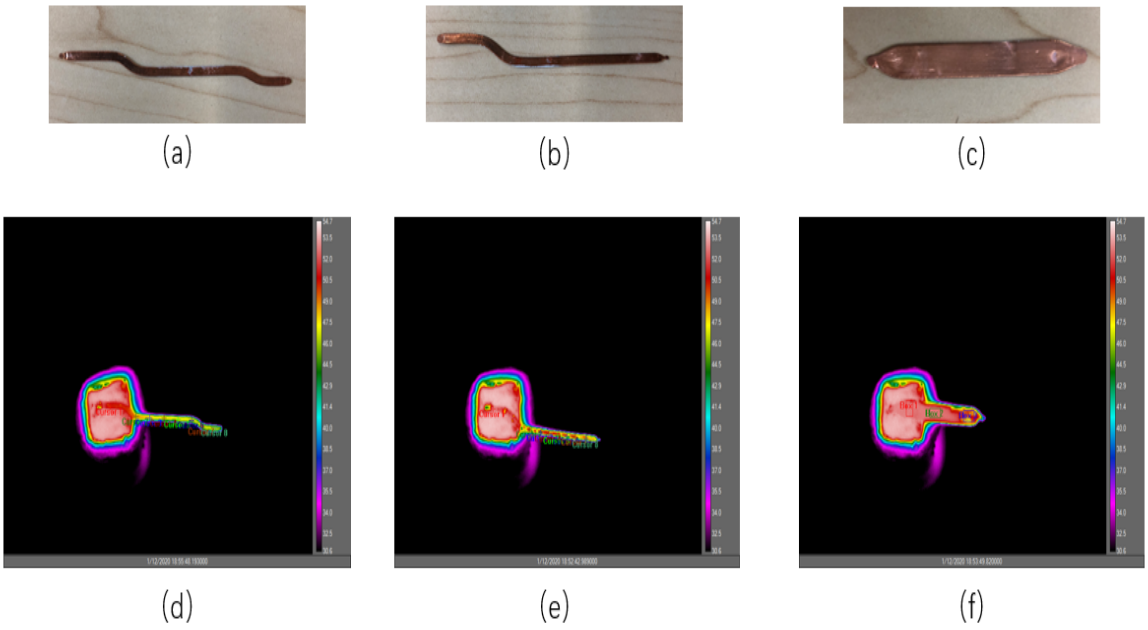

Figure 3.2(a) Samsung S8 heat pipe (S8), (b) Samsung S7 heat pipe (S7), (c) Commerical heatpipe (S1), (d) IR image of S8 sample under 13V power input, (e) IR image of S7 sample under 13V power input, and (f) IR image of S1 sample under 13V power input. IR image can effectively identify the temperature reading at a location, which should be highly accurate. The cursors, on the image, are the temperature reading point.

3.1.2 External Factor Experiment Verification

To make sure the measurement of thermal conductivity of three heat pipes, an external factor experiment verification was performed first. A copper plate with 1 inch in width, 4

inch in length, and 0.25 inch in thickness was tested by this experimental setup. During the experiment, it has been found that the temperature reading of the copper plate couldn't remain a constant over 40 minutes. There is a small positive slope, as shown in figure 3.3 (a). This might be caused by that the cooling method can not remove the heat flux that went through the copper plate. However, the temperature difference between the measurement point, which refers to the ΔT, remains a constant after 4 minutes, as shown in figure 3.3 (a). Conclusively, the ΔT indicates if the system reaches the steady state. Another test is also performed to verify this idea. As shown in figure 3.3 (b), the ΔT is a constant after 5 minutes. Using the aforementioned equation (3.1) and (3.2). The thermal conductivity of the copper plate is calculated. The results are 439.57 W/mK and 387.85 W/mK for voltage of 16V and 19V respectively. Generally, the pure copper thermal conductivity is 400 W/mK. Therefore, the error of this experiment set up is around 3.4%, which is less than 5%. It proves that this experiment set up could be used to calculate the thermal conductivity of the heat pipes.

3.2 Result and Discussion

3.2.1 External Experiment Results and Discussion

In the experiment, three heat pipes are tested: Samsung S7 heat pipe (S7), Samsung S8 heat pipe(S8), and a commercial heat pipe (S1) as shown in figure 3.2. Three smartphone heat pipe tests paved the way to design the polymer vapor chamber since the test results set the minimum vapor chamber thermal conductivity requirement of the polymer vapor chamber design. The dimension of the samples is shown in table 3.1. To investigate the effects of the external factors, the voltage supplied to the cartridge heater is selected from 10V to 16V; the cooling condition is selected from 10 C to 20 C; the angle between the heat pipe and the

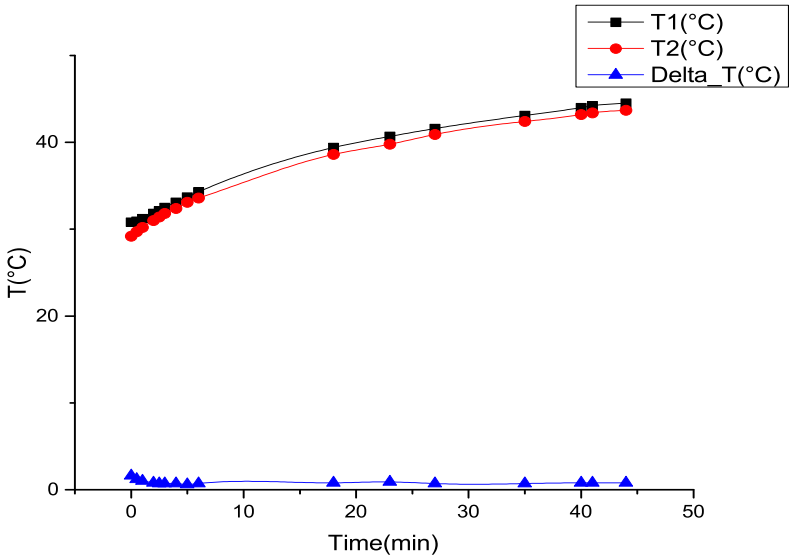

(a) 16V

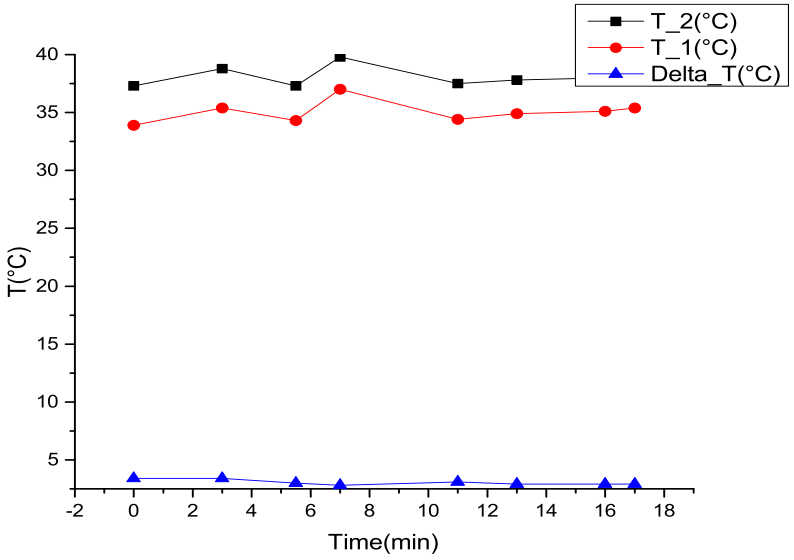

(b) 19V

Figure 3.3 Copper Sample temperature reading profile. (a) temperature prfoile at cartridge heater is supplied with 16V. (b) temperature profile at cartridge heat is supplied with 19V. The temperature reading could not remain constant since the heat flux input is greater than the heat removal. The temperature also fluctuates because the thermal couple does not contact with the sample well.

horizontal plane is selected from 0 degrees to 90 degrees.

The thermal conductivity results are summarized in table 3.2 and figure 3.4.The test results show that the thermal conductivity of the vapor chamber sample is not a constant. Under different conditions, the vapor chamber has different performances. Figure 3.4 shows, the S1 sample has its maximum thermal conduction at test 4 where it has low heat input, low heat

Table 3.2
Test Condition

Test Run	Source Voltage(V)	Sink temperature(°C)	Angle (°)
1	16	10	90
2	16	20	90
3	10	10	90
4	10	20	90
5	16	20	0
6	10	10	0
7	16	10	0
8	10	20	0

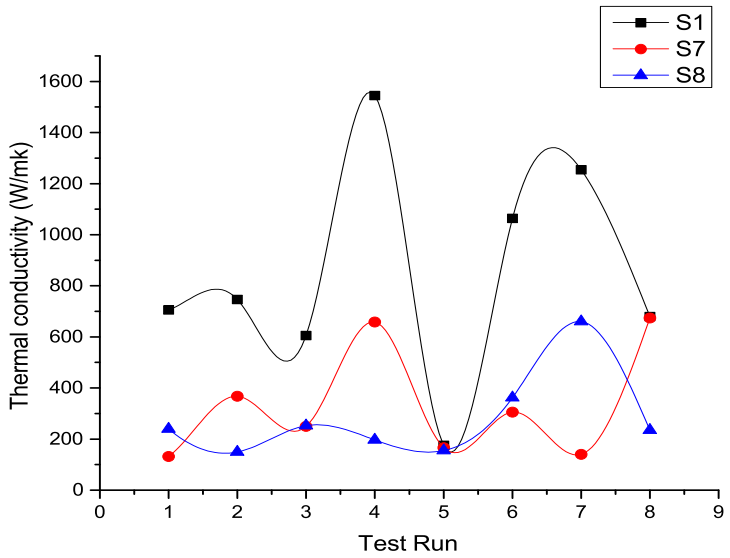

Figure 3.4 Thermal conductivity of three heat pipes. Unlike the metal material, the thermal conductivity of the heat pipes are expected to fluctuate around a certain value. This figure showed that the S1, S7, and S8 had a mean thermal conductivity about 800 $W/m \cdot K$, 300 $W/m \cdot K$, and 250 $W/m \cdot K$, respectively.

sink temperature, and vertical placement. The vertical placement might help the liquid rewetting the evaporator section since the evaporator is at the bottom, as the angle equals 90 degrees. The S7 sample has its maximum thermal conduction at test 8 where it has low heat input, low heat sink temperature, and held horizontally. However, the result of test 4 run of S7 sample has the second largest thermal conductivity. It also indicates that gravity can help the rewetting process. The S8 sample has its maximum thermal conduction at test 7 where it has high heat input, high heat sink temperature, and held horizontally. The results show that the samples can not have high heat flux and high heat sink temperature at the same time since the test run 5 shows that the three samples have low thermal conductivity.

Moreover, the vapor chamber does not have a stable performance but has an average thermal conductivity of about 800 $W/m \cdot K$, 300 $W/m \cdot K$, and 250 $W/m \cdot K$ for S1, S7, and S8, respectively. Here, it is worthy to note that the S8 sample had thermal conductivity around 600 $W/m \cdot K$ at the beginning test. After several tests, the thermal conductivity of the S8 sample dropped dramatically to 250 $W/m \cdot K$. This thermal conductivity drop might be caused by that the S8 sample was bent accidentally. It might cause the deformation of the internal structure since no crack could be found on the surface of the S8 heat pipe. Moreover, such deformation is irreversible. It might explain that the thermal performance of S8 is much worse than that of S1 and S7. Conclusively, the material elasticity should also be considered to avoid that the vapor chamber can not function due to plastic deformation.

3.2.2 Design Expert Analysis on the Results

Moreover, it can't directly tell which one has the greatest influence. Therefore, the results are further processed in the Design Expert 11, which can generate P-value to determine which factor has the great influence.

As the data put in the Design Expert 11, the Box-Cox plot shows that the lambda is out

of CI lambda. It indicates that the model requires transformation. After several trails, the nautrual log transformation is used since the lambda is within the CI lambda and close to the best lambda, as shown in figure 3.5.

In the Design Expert 11, the natural log transformation model was selected to investigate the P-value of each external factors. As shown in figure 3.6, the half normal plot indicates that the factor heat pipe has the largest effect in determining the thermal conductivity. It means that the vapor chamber design has the greatest influence on the smartphone heat pipe thermal conductivity. This result matched with previous researcher funding that at different heat source input, the thermal coductivity of heat pipe or vapor chamber changed [1-15] The source term, which determines the input heat flux, has the second greatest effect. Furthermore, the p-values of interaction terms (AB, BC, CD) also show that the interaction terms are significant. Here, the sink factor is not siginificant. However, Yong Li et al. recently showed that the vapor chamber thermal conductivity can be significantly affected by the cooling condition [40]. They showed that at 303K and 323K cooling water, the critical heat flux of copper foam vapor chamber can reach 180 W/cm^2, which increased 100-200 % compared to that of copper mesh vapor chamber. However, in this work, the water cooling temperature did not affect the heat pipe thermal performance. This contradiction might be caused by that the water cooling temperature is less than 303K. Further investigation is needed.

Conclusively, the effective thermal conductivity of the heat pipes is mostly affect by the heat pipe designs, which relate to the size, the internal structure, and the material etc. Besides this, it has been found that the gravity improve the thermal conductivity of the heat pipes by placing them vertically since the rewetting process is facilitated in this case. Therefore, the smartphone might have its chip set at the bottom to improve the effective thermal conductivity of the heat pipes. As the heat source power increased, the effective thermal conductivity of the heat pipe can decrease or increase, which is hard to predict. However, it

should fluctuate around its mean thermal conductivity.

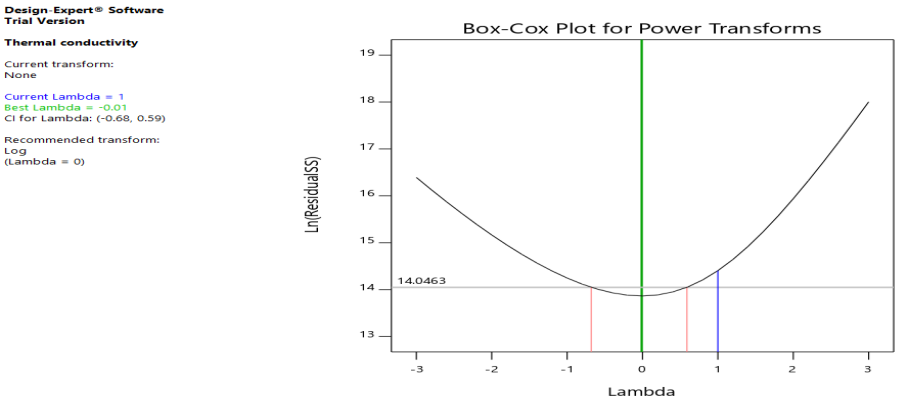

(a) No-transformation

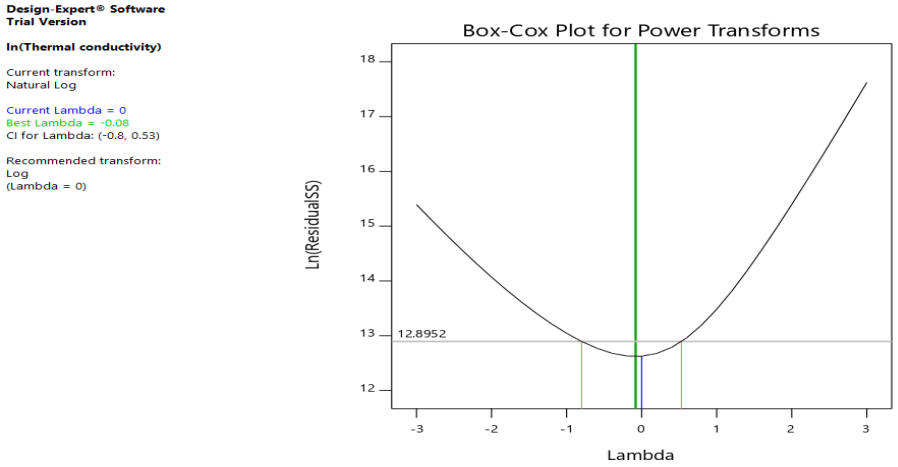

(b) Natural log transformation

Figure 3.5 Box-Cox plot: the Box-Cox plot is used to transform the non-normal distribution data to normal distribution data, so that the variance can be stabilized. (a) Non transformation Box-Cox plot. It shows that the lambda is outside the CI lambda, which indicates transformation required. (b) Natural log transformation Box-Cox plot. It shows that the model is normal distributed and stabilize the variance, where the current lambda of 0 is close to the best lambda of - 0.08. A model has Lambda close to the best Lambda, which means that the Design Expert 11 can predict the model well.

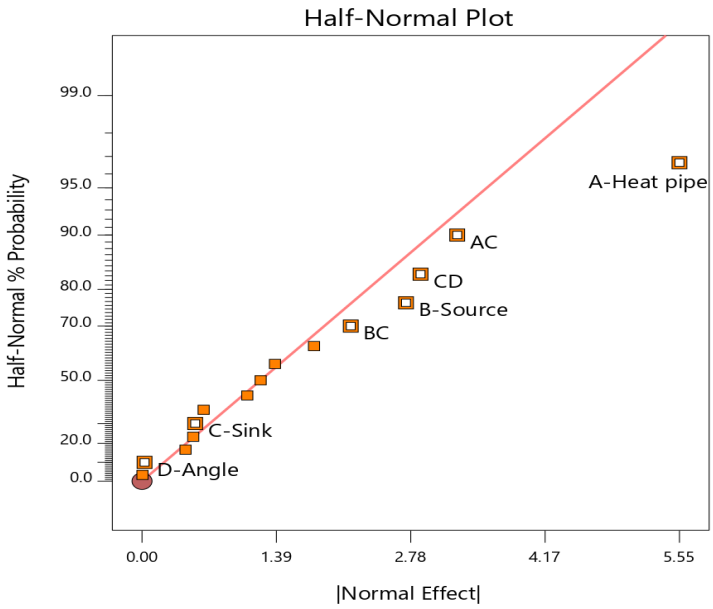

Figure 3.6 Half normal plot: factor that is far away from the line should be considered as important. However, after the factor selection, the line coule be changed. At the end, the factor A is the most important factor. Factor B is the second most important factor.

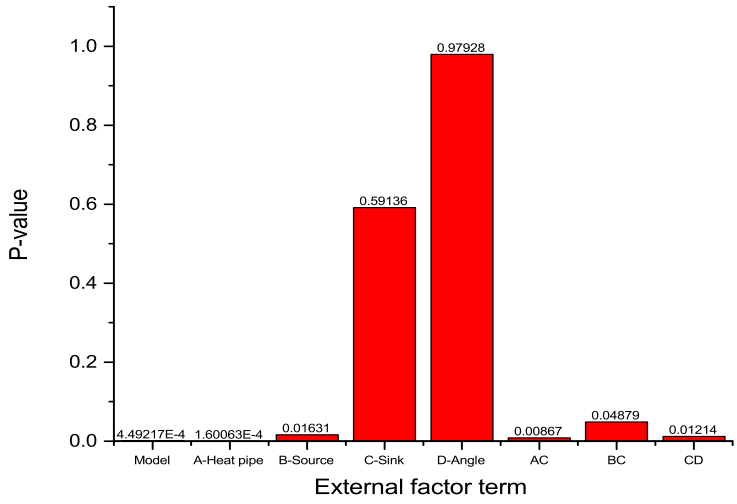

Figure 3.7P-value plot: the factor term should be considered as important as its P-value less than 0.05; Here, the model has p-value 0.000449, which is less than 0.005. It shows that the model is significant to study. Factor A (heat pipe) has p-value 0.000160, which is lowest p-value factor. Factor B (heat source) has p-value 0.0163, which is second lowest p-value factor. Interaction factor AC (heat-pipe and sink), BC (heat source and sink), and CD (sink and angle) have p-value 0.00867, 0.04879, and 0.01214, respectively. These factors and interaction factors are important, which affects the vapor chamber thermal conductivity. Among them, the heat pipe design has the greatest influence.

Chapter 4

Internal Factor Computational Study and Result

The vapor chamber is composed of porous media. To improve the CHF and thermal conductivity of the vapor chamber, it is to increase the capillary pressure and separate the vapor and liquid phase. Byon et al. showed that bi-porous media can improve the capillary pressure dramatically [5]. To obtain the best capillary performance, the ratio between the particle diameter and the cluster size should within 0.17 and 0.29 so that the liquid and the vapor can propagate in the small pore and large pores, respectively. Wen et al. designed a two level-hierarchical surface, where the bubble nucleation occurred only at microcavities.[27]. Their design achieved rapid rewetting and high-frequency bubble departure so that the critical heat and heat transfer rate increased 16% and 46% compared to the plain copper surface. Shaeri et al. manufactured a copper-based biphilic vapor chamber and showed that the biphilic vapor chamber had a higher critical heat flux than the hydrophobic vapor chamber [22]. Conclusively, the thermal conductivity of the vapor chamber depends on the evaporation or boiling rate and rewetting speed. Based on this idea, a multi-layer porous media study with central heating and upper natural cooling vapor chamber is designed in Ansys, as shown in

figure 4.1.

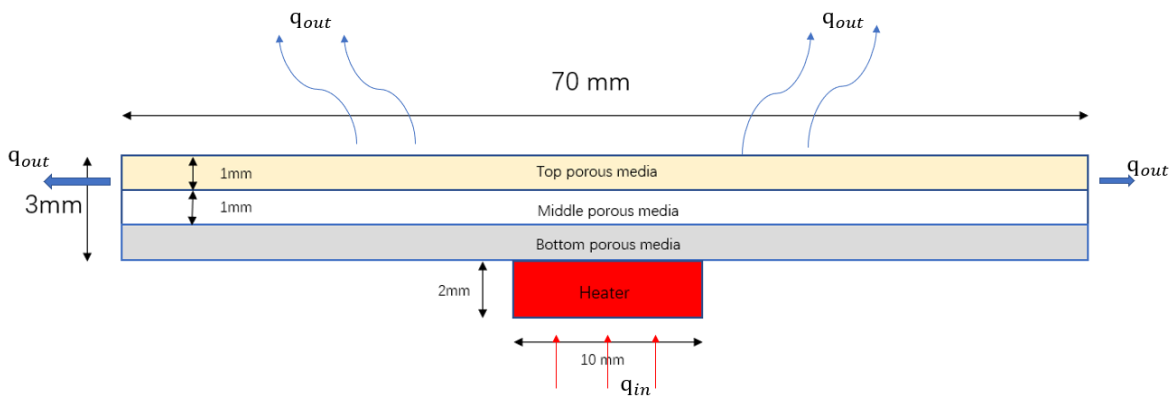

Figure 4.1 Three-layer 2-D vapor chamber model: the dimension of the vapor chamber is designed based on the Samsung S7 heat pipe dimension with height 3mm and length 70mm. The heater is to simulate 1cm*1cm chip with input heat flux 10 W/cm^2. In CFD model, the entire mesh element size is set to $3e^{-4}$ m. The heater was applied with 10 W/cm^2 heat flux at the bottom, which heated up the entire model. The liquid and vapor inside the vapor chamber absorbed the heat and moves under the pressure difference. Then, the top and lateral wall of the model is set with air cooling, where the convection coefficient is 100 $W/K \cdot m^2$ and air temperature is 300K so that $q_{out} = hA(T_{wall} - T_{air})$. The detailed parameters are summarized in table 4.2.

4.1 Model Verification

If the model is correct, the continuity residual should be small. In this work, each model test had to satisfy the continuity residual less than 10^{-5}. As shown in figure 4.2, the continuity residual is around 10^{-9}. It shows that the model is correct.

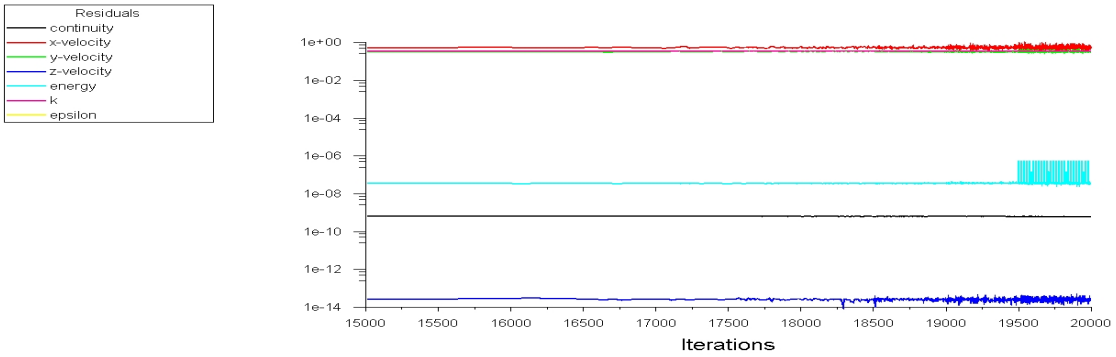

Figure 4.2 Residual plot of the test 1. It shows that the continuity, energy, and z-velocity residuals are less than 10^{e-5}. Velocity residuals at x and y direction are about 10^{-1}, which could be considered as a small number since the velocity inside the model is very small. Therefore, the model is converged.

4.2 Porous Layer Study

The bottom is set a copper block with heat flux input 10 W/cm^2, and the boundary condition is set to be natural convection with heat transfer coefficient 100 $W/K \cdot m^2$ and air temperature 300 K. In this case, the liquid used is incompressible liquid water with filling ratio 0.7. In total, 8 tests are performed and their boundary condition and initial condition are summarized in table 4.1 and 4.2.

The test results are plotted in figure 4.3. Test 1, test 2, and test 3 results verify the idea that the multi-layer porous media vapor chamber, with the highest porosity at top and the lowest porosity at the bottom, can improve the thermal conductivity. From the plot, the temperature difference of test 1 is lowest among the three tests and reaches 14.8 K. However,

Table 4.1
Ansys Test Condition

Test Run	Top Layer Porosity	Mid Layer Porosity	Bottom Layer Porosity
1	0.8	0.6	0.4
2	0.4	0.6	0.8
3	0.8	0.6	0.8
4	0.4	0.6	0.4
5	0.3	0.6	0.3
6	0.2	0.6	0.2
7	0.1	0.6	0.1
8	0	0	0
9(NG)	0.4	0.6	0.8

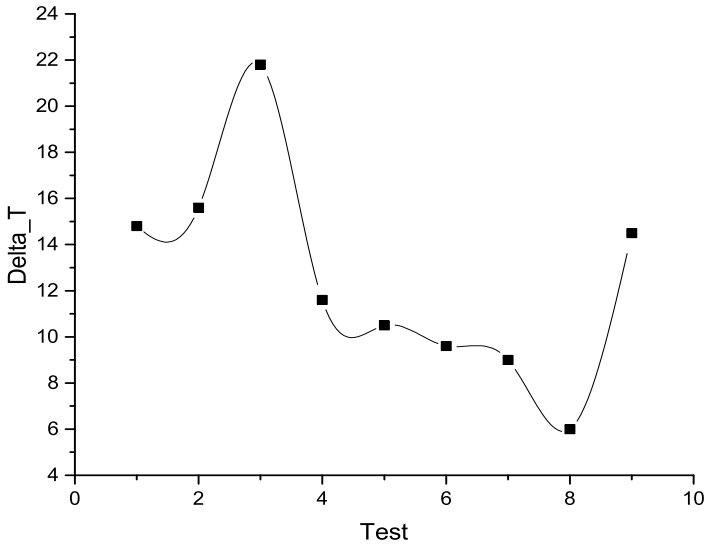

Figure 4.3 The temperature difference between the highest and the lowest temperature for each test. Through changing the porosity of the porous media layer, the temperature difference can vary. This figure shows that the temperature difference is decreasing from test 3 to test 7 by decreasing the top and bottom layer porosity. The test 1 and test 2 results show that the temperature difference is slightly affected by turning upside down. The test 8 is the pure copper plate test, which has the lowest temperature difference. The test 9 with the gravity and test run 2 without the gravity results show that the gravity has little effect on the temperature difference of the model.

Table 4.2
Boundary Condition and Inital Condition

	$q_{in}(W/cm^2)$	$T_{surrounding}(K)$	$h_{air}(W/K \cdot m^2)$	$K_{copper}(W/m \cdot k)$	$T_{initial}(K)$
All test	10	300	100	387.6	300
	$T_{sat}(K)$	$P_{sat}(MPa)$	$h_{fg}(J/kgmol)$	$\mu_f(Kg/m \cdot s)$	$\mu_g(Kg/m \cdot s)$
Fluid initial property	333	20	2357.7	$1.003e^{-3}$	$1.34e^{-5}$

the temperature of test 2 reaches 15.6 K. The temperature difference improvement is 0.8 K. It indicates that multiple-layer porosity with by using descending porosity arrangement to improve the thermal conductivity of a vapor chamber might not be efficient. From test 3 to test 7, the central porous media has a fixed porosity 0.6, and the top and bottom porous media have porosity value from 0.8 to 0.1. Figure 4.3 shows that the temperature difference is 21.8 K, 11.6 K, 10.5 K, 9.6 K, and 9 K for test 3, test 4, test 5, test 6, and test 7, respectively. It is a decreasing trend from test 3 to test7. Test3 has porosity values of 0.8, 0.6, and 0.8 for the top, middle, and bottom porous media. Test4 has porosity value 0.4, 0.6, and 0.4 for the top, middle, and bottom porous media. By lowering the top and bottom porosity value, the temperature difference can decrease 10.2 K. The decrease is actually caused by increasing the capillary pressure. Conclusively, the vapor chamber wick structure should have its highest porosity at its central part. Furthermore, the top and bottom porous media should have lower porosity value than the central porous media for multi-layer vapor chamber design.

4.3 Nucleation Performance Analysis

To further improve the thermal performance of a vapor chamber, the nucleation sites of each test are also investigated. Figure 4.4 shows that each test has its nucleation site at a different time frame. The test 7, 6, 5, 4, 3, 2, and 1 start boiling nucleation at time frame 535, 510, 500, 480, 371, 415, and 425, respectively. The reason is that the bottom temperature boundary condition reaches 335 K. Based on Lee's model, as the temperature reaches the saturation temperature, the evaporation and condensation could occur. In this case, the internal energy of this system increasing all the time so that the evaporation process is dominant. As the temperature is over the saturation temperature for a while, the vapor bubbles merge and the vapor film form, as shown in figure 4.4 and 4.5. Moreover, as all the liquid turns to vapor, the dry-out phenomenon occurs. And the vapor chamber no longer functions. Such

a vapor chamber can overheat the chip. Conclusively, the dry-out phenomenon caused by the temperature exceeds the saturated temperature for a long time, where the temperature can not be cooled down. To prevent it happens, the electronic device should monitor its own temperature. As the temperature exceeds the saturated temperature for a long time, the device should lower its own power output by warning its users. In fact, improving the cooling condition can also prevent the dry out by facilitating the condensation process.

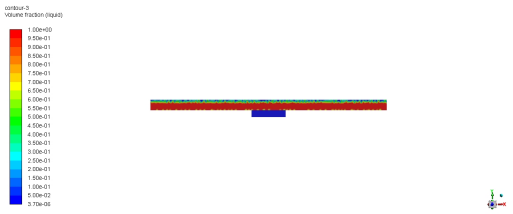

(a) Test1 220 frame

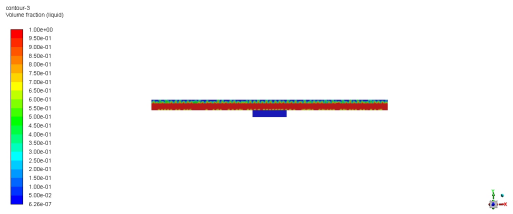

(b) Test3 220 frame

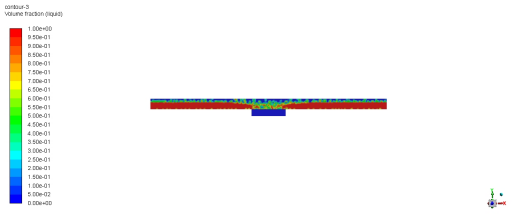

(c) Test1 450 frame

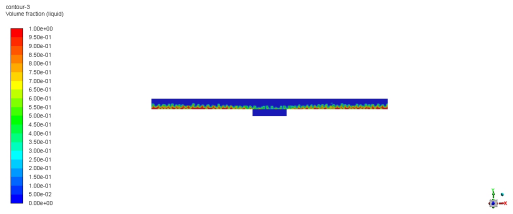

(d) Test3 450 frame

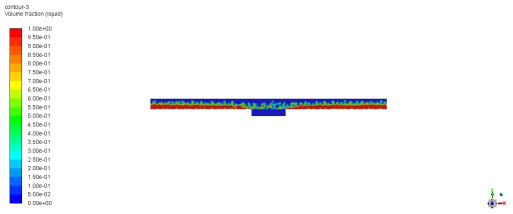

(e) Test1 480 frame

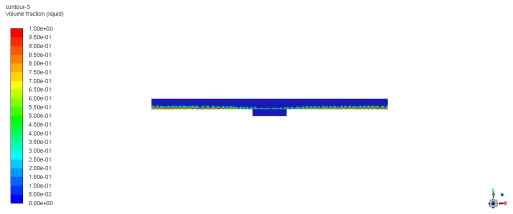

(f) Test3 480 frame

Figure 4.4 Liquid volume distribution of boiling nucleation simulation: (a) test 1 220 frame liquid volume distribution, (b) test 3 220 frame liquid volume distribution. Initially, at the low-temperature boundary condition, the liquid volume distribution of test 1 and test 3 are similar. (c) test 1 450 frame liquid volume distribution, (d) test 3 450 frame liquid volume distribution. After 230 frames, much less water remained in test3 than test 1. Test 3 had dry-out phenomenon, (e) Test 1 480 frame liquid volume distribution, and (f) test 3 480 frame liquid volume distribution. After 30 frames, the evaporation process starts to be dominant in both tests. The test 1 multi-layer design has much better thermal performance than that of test 3. At 220 frame, test 1 and test 3 have 37 and 40 yellow bubble sites outside the evaporation section, respectively. Those sites might be bubble nucleation sites, which can hinder the rewetting process.

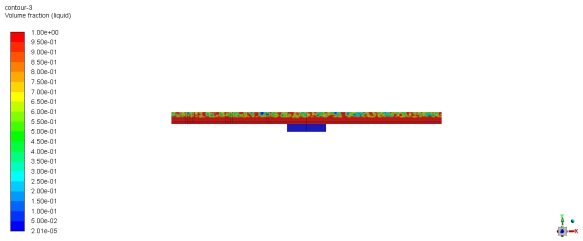

(a) test 7 450 frame

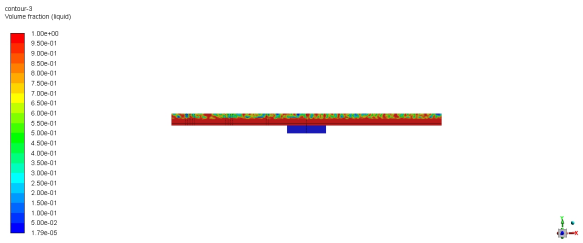

(b) test 7 510 frame

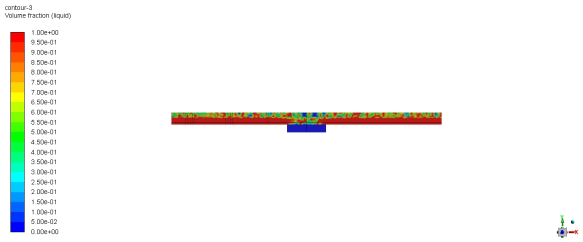

(c) test 7 535 frame

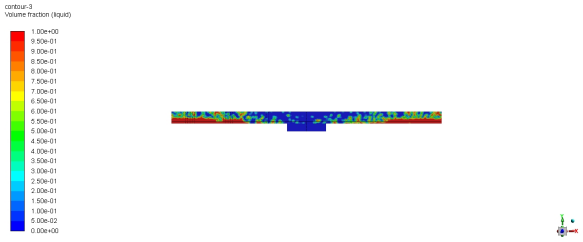

(d) test 7 580 frame

Figure 4.5 Liquid volume distribution of boiling nucleation simulation: (a) test 7 450 frame liquid volume distribution: the model at the frame where the test 3 and 1 had boiling nucleation occurrence, (b) test 7 510 frame liquid volume distribution: the model at the frame where the test 3 and 1 had partial dry-out phenomenon occurrence, (c) test 7 535 frame liquid volume distribution: the model at the boiling nucleation, and (d) test 7 580 frame liquid volume distribution: the model had partial dry-out phenomenon. The evaporation or boiling nucleation process is not dominant until 535 frame. It takes 100 frames more to reach the boiling nucleation compared to the test 1. Thus, it showed that the porous media porosity change can postpone the boiling nucleation and dry-out occurrence. Furthermore, at 580 frame, there are 3 bubble nucleation sites outside the evaporator section, where the local liquid density is reduced to 0. Those sites hinder the rewetting process.

To further improve the thermal performance of the vapor chamber, the nucleation sites should be regulated to avoid non-uniform pressure distribution, which might be caused by vapor or liquid can not propagate through the pores. So it is significant to keep the boiling nucleation sites at a certain location. As figure 4.4 and 4.5 show, the boiling nucleation sites can be kept at evaporator. However, the figures also show that there are small vapor bubbles trapped at the bottom surface. These bubbles could be removed by changing the surface energy of the surface.

Replacing the uniform wettability of the wick structure with a biphilic wick structure, which contains hydrophobic and hydrophilic surface, can improve the fluid dynamic motion [2]. Betz et al. constructed hydrophilic, hydrophobic, superhydrophilic, superhydrophobic, and superbiphilic wick structure surface through nano-structuring process, microlithography, and thin hydrophobic polymer coating, as following. They tested those surface structure performance by using pool boiling test, and found that a vapor film was formed before any vapor bulb departed from the hydrophobic and superhydrophobic surfaces at a low critical heat flux; some nucleation sites were found on the hydrophilic surface but they did not merge to a vapor film; vapor film could only be found on the superhydrophobic part of the superbiphilic wick structure, and the superhydrophilic part of the superbiphilic wick structure remains completely wet. Through these experiment phenomena and their calculation results, they concluded that the super-biphilic design delayed the critical heat flux and increase the heat transfer coefficient two and four times larger than the heat transfer coefficient of the superhydrophillic, and the superhydrophobic design [2]. Shaeri et al. manufactured copper based biphilic vapor chamber and showed that the biphilic vapor chamber had a higher critical heat flux than the hydrophobic vapor chamber. They also found that increasing the filling ratio reduced the thermal resistance of the biphilic vapor chamber [22]. Ji et al. found that alternating the wettability of the evaporator of their vapor chamber can keep nucleation sites at certain places and increase the heat transfer coefficient. They also reported that increasing the well-organized nucleation sites helps the fluid flow transportation, which improves

thermal performance [36]. A flow boiling simulation to mimic the case inside the evaporator wick is also performed to demonstrate the importance of the surface energy, as shown in figure 4.6. As the bottom surface is hydrophobic, where the contact angle (CA) equals to 160 degrees, the vapor density of CA = 160 degrees on the bottom surface is less than that of CA = 90 degrees. Thus, the vapor can be removed by the rewetting liquid.

In summary, the thermal conductivity of the vapor chamber can be improved by regulating the wettability of its wick structure and vapor channel. The reason is that wettability alternation on the surfaces can keep the boiling nucleation at certain sites and facilitate the rewetting process.

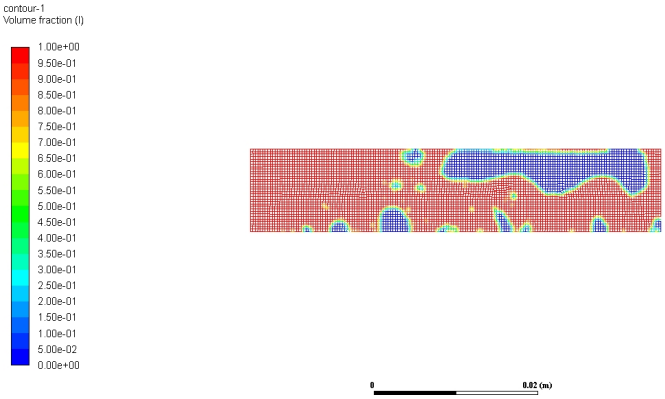

(a) contact angle = 90

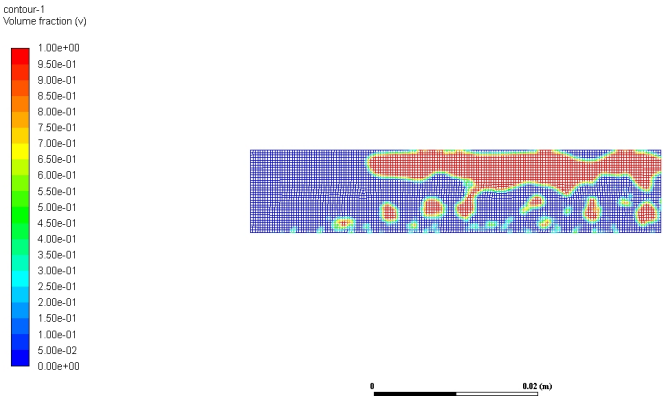

(b) contact angle = 160

Figure 4.6 Flow boiling simulation with different contact angles: (a) as contact angle = 90, the vapor is likely to stick on the bottom surface. There are 10 bubble nucleation sites, which occupies at least 1/4 bottom surface. (b) as contact angle = 160, the vapor could be easily removed with the replenishment liquid flow. There are 13 bubble nucleation sites, which occupy 1/10 bottom surface area. Furthermore, the bottom vapor density is less in figure 4.6 (b) than in figure 4.6 (a) because case (b) has a hydrophobic surface.

4.4 With and Without Gravitation Liquid and Temperature Distribution

In the external factor study, the horizontal and vertical test has shown that the gravitational force can increase the vapor chamber or heat pipe thermal performance since it facilitates the rewetting process. In other words, the gravitational force might not be required for the horizontal test. Therefore, an unrealistic model is tested without the gravitational force, which is test 9. The test 9 has the same parameters as the test 2 except the gravity. It turns out that the thermal performance of the test9 is better than that of test 2.

Figure 4.7 and Figure 4.8 show the liquid and vapor distribution of the test9 and test 2, respectively. Compared to the liquid volume distribution of the test 9 , that of the test 2 has a higher liquid density at the bottom. The test 9 has a uniformly distributed liquid density over the entire surface. Moreover, in the test 9, the vapor bubble merged to the vapor film. They vapor film stays at the bottom surface and can't be raised to the condensation section, as shown in figure 4.7 (b). In test 2, the vapor bubble can be raised up to the condensation, as shown in figure 4.8 (b). In other words, the test 9 has an n-shape liquid volume distribution. The test 2 has a v-shape liquid volume distribution. From this point, it seems that the capillary pressure performance of test 2 should be better than that of test9. It means that the temperature difference of test 2 should be lower than that of test 9. The highest temperature of test 9 is 379.6 higher than that of test 2 by 1.3 K. However, it turns out that the result contradicts to the capillary pressure performance result, where ΔT_{test9}= 14.5 K< ΔT_{test2} = 15.6 K. Thus, the gravity does affect the vapor chamber as it has been placed horizontally. However, it required more test runs to verify that the gravity can facilitate or hinder the liquid and vapor transportation inside the vapor chamber.

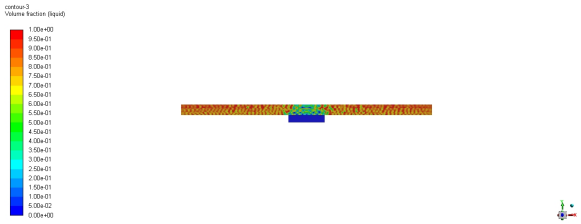

(a) Test9 450 frame

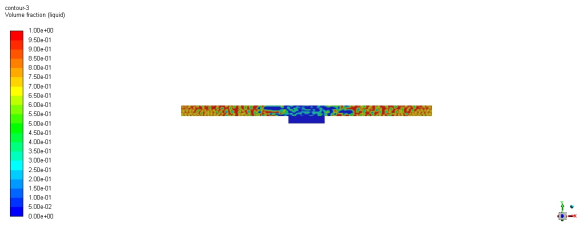

(b) Test9 474 frame

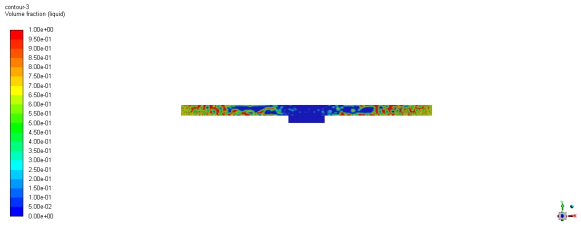

(c) Test9 504 frame

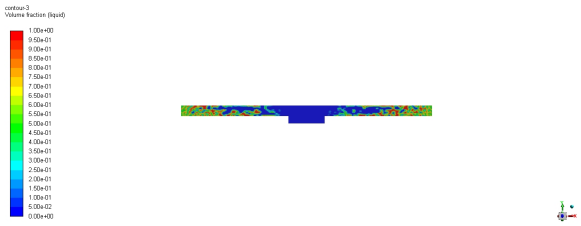

(d) Test9 534 frame

Figure 4.7 Liquid volume distribution of boiling nucleation simulation: (a) test 9 450 frame liquid volume distribution: the model before the boiling nucleation happens, (b) test 9 474 frame liquid volume distribution: the model at boiling nucleation, (c) test 9 504 frame liquid volume distribution: zero liquid density could be found at evaporator section, and (d) test 9 534 frame liquid volume distribution: the liquid could not be transported back to the evaporator section. Without the gravity, the buoyance force is not considered so that the liquid phase could be everywhere rather than concentrated on the bottom surface. On the other hand, without the gravity, the vapor phase could stay at the bottom rather than concentrated on the top surface. As the heat flux applied to the bottom copper block, the liquid evaporated to the vapor and caused the pressure at the center was higher than the pressure at the sides. Therefore, the liquid phase could never be transported back to the evaporator section.

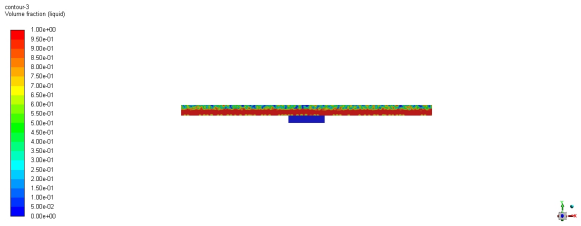

(a) Test2 424 frame

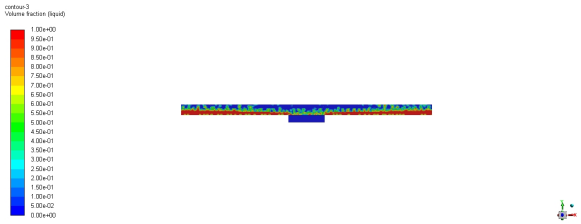

(b) Test2 474 frame

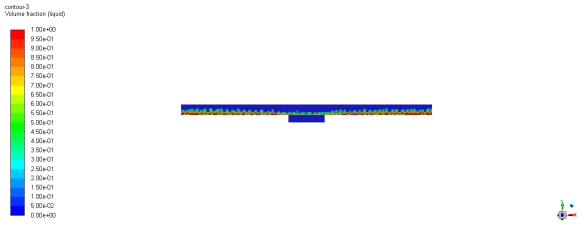

(c) Test2 504 frame

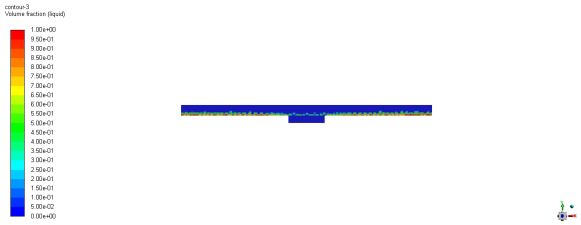

(d) Test2 534 frame

Figure 4.8 Liquid volume distribution of boiling nucleation simulation: (a) test 2 424 frame liquid volume distribution: the model before boiling nucleation happens, (b) test 2 474 frame liquid volume distribution: the model at boiling nucleation occurring, (c) test 2 504 frame liquid volume distribution: the liquid could be transported back to the evaporator section, and (d) test 2 534 frame liquid volume distribution: partial dry-out phenomenon occurs. With gravity, the liquid and vapor could be concentrated at the bottom and top surface, respectively. The liquid phase could be transported back to the evaporator section.

4.5 Polymer Vapor Chamber and Heat Pipes

The aforementioned section investigated the external and internal factor effects on the thermal conductivity of the vapor chambers. Besides those factors, the material of the vapor chamber also plays a big role in determining the thermal conductivity of the vapor chamber. In chapter1, it has been noted that most of the vapor chambers are made of metal since metal material has high thermal conductivity. However, the massive production of the metal vapor chambers could be expensive. Furthermore, the metal vapor chamber does not apply to high sensitivity electronic devices. Therefore, polymer material, recently, had received a lot of attention due to its cheapness, high corrosion resistance, and flexibility. However, in recent research reports, the thermal conductivity of the polymer material has not been competitive with the metal material. In 2019, Hou et al. found that adding carbon fiber into polydimethylsiloxane(PDMS) can enhance the thermal conductivity of PDMS to 6.04 $W/m \cdot K$ [38]. In 2019, Han et al. fabricated a high thermal conductive BNNS/epoxy composite with a nacre-mimetic 3D filler network, which has a thermal conductivity of 6.07 $W/m \cdot K$ [13]. In 2018, Zhu et al. fabricated BNNS/TPU nanocomposites film, which has an in-plane thermal conductivity of 14.7 $W/m \cdot K$. They also reported that adding BN to PDMS can have the highest thermal conductivity of 22.5 $W/m \cdot K$ [44]. These foundings show that although the thermal conductivity of polymer material is improved, polymer material, at the current stage, can not replace metal as the conductive material.

There are some existing polymer vapor chamber and heat pipe designs. In 2013, Oshman et al. fabricated one of the highest thermal conductivity polymer heat pipes, which has a thermal resistance of 0.66 K/W [8]. This design used aluminum material to make a wick structure. They also reported that the polymer case replaced by the copper foil case can decrease 4.6 times in thermal resistance. In 2015, Yang et al. fabricated a novel flat polymer heat pipe with thermal via, which has the lowest thermal resistance of 3.7 K/W [15]. In 2018, Lim and Kim fabricated a polymer-based flexible pulsating heat pipe, which has the lowest

thermal resistance of 2.41 K/W [14]. In 2019, Hao et al. fabricated polytetrafluoroethylene(PTFE) based oscillating heat pipes, where its lowest thermal resistance of 0.0092 K/W [34]. However, the non-condensable gas can penetrate the PTFE so that such an oscillating heat pipe has a short life-time. These designs showed that the polymer-based vapor chamber and heat pipes had the potential to replace metal-based that.

Chapter 5

Conclusion and Future Work

In this work, the internal and external factors that affect the thermal conductivity of the vapor chamber are investigated. The current experiment setup can test out the thermal conductivity of the heat pipe within 5% error. However, the cooling method can not remove the heat generated by the cartridge heater, which results that the temperature of the sample could not remain constant. From the experiment result, it can not directly tell which external factors affect the vapor chamber thermal performance most. With Design Expert 11, it has been found that vapor chamber design has the greatest effect; Heat source power has the second-largest effect. Gravitation could facilitate the rewetting process only if the vapor chamber was held vertically and its evaporation site was at the bottom.

In chapter 4, it has been found that the multi-layer porous media can affect the thermal performance of the vapor chamber. The best design for a multi-layer is to have the largest porosity at the center of the wick structure. Furthermore, to increase the bubble departure frequency or to have less vapor density on the bottom surface, the bottom surface is required to be hydrophobic. Another method to achieve this goal is to use microcavity at the evaporator section. Moreover, the bi-porous media can increase the capillary pressure inside the

liquid-wick structure so that the rewetting process can be facilitated. At the current stage, polymer material still has low thermal conductivity. Therefore, a vapor chamber composed of polymer material should have metal material as its wick structure. The polymer oscillating heat pipe shows great thermal conductivity. However the non-condensable can penetrate the polymer material resulting in a short-life cycle.

Future work is needed to investigate the bi-porous media with micro-cavities in the wick structure. Bi-porous media could provide high capillary pressure and micro-cavities, which can keep the boiling nucleation at certain sites. It is expected that such a design can speed up the rewetting process. Conclusively, improving the liquid and vapor motion is another key to improve the thermal conductivity of the vapor chamber.

Bibliography

[1] Yuji Saito Ahamed Shahed. High Performance Ultra Thin Heat Pipe Cooling Module for Mobile Hand Held Electronic Devices, 2017.

[2] Amy Betz, James Jenkins et al. Boiling heat transfer on superhydrophilic, superhydrophobic, and superbiphilic surfaces. *International Journal of Heat and Mass Transfer*, 157:733,41, 2013.

[3] Ansys. The pressure-based segregated algorithm, 2009.

[4] Theodore L. Bergman. *Fundamentals of Heat and Mass Transfer, 8th Edition*. 2013.

[5] Chan Byon, Sung Jin Kim et al. Capillary performance of bi-porous sintered metal wicks. *International Journal of Heat and Mass Transfer.*, 55:4096,4103, 2012.

[6] Gaurav Soni Changsong Ding. A flat heat pipe architecture based on nanostructured titania. *JOURNAL OF MICROELECTROMECHANICAL SYSTEMS*, 19(4):878–884, 2010 Aug.

[7] Chen Li Ronggui Yang Christopher Oshman, Bo Shi. The development of polymer-based flat heat pipes. *JOURNAL OF MICROELECTROMECHANICAL SYSTEMS*, 20(2):410–417, 2011.

[8] Qian Li Christopher Oshmean. Flat flexible polymer heat pipes. *Journal of Micromechanics and Microengineering*, 2012 Nov.

[9] Eric Pop. Energy dissipation and transport in nanoscale devices. *Nano Res*, 3:147,169, 2010.

[10] G. Moore. The future of integrated electronics. *Fairchild Semiconductor internal publication*, 2, 1964.

[11] Jeongmin Lee, Lucas E. O'Neill, eunghyun Lee, Issam Mudawar. Experimental and computational investigation on two-phase flow and heat transfer of highly subcooled flow boiling in vertical upflow. *International Journal of Heat and Mass Transfer*, 130:83,92, 2018.

[12] JIANNAN TAN, B.S. A study of solving navier-stokes equations with a finite volume method based on polygonal unstructured grids and the computational analysis of ground vehicle aerodynamics, 2010.

[13] Jinkai Han, Gaolai Du, Weiwei Gao, and Hao Bi. An anisotropically high thermal conductive boron nitride/epoxy composite based on nacre-mimetic 3d network. *Advanced Functional Materials*, 29:1900412–1,1900412–9, 2019.

[14] Jonghyun LimSung Jin Kim. Fabrication and experimental evaluation of a polymer-basedflexiblepulsating heat pipe. *Energy Conversion and Management*, 156:358,364, 2018.

[15] Kai-Shing Yang, Tsung-Yi Yang, Cheng-Wei Tu et al. A novel flat polymer heat pipe with thermal via for cooling electronicdevices. *Energy Conversion and Management*, 100:37,44, 2015.

[16] Kyung Mo KimYeong Shin JeongIn Cheol Bang. Thermal analysis of lithium ion battery-equipped smartphoneexplosions. *Engineering Science and Technology, an international Journal*, 22:610,617, 2019.

[17] Li-Anne Liew, Ching-Yi Lin, Ryan Lewis, Susan Song, Qian Li, Ronggui Yang, YC lee. Flexible thermal ground planes fabricated with printed circuit board technology. *Journal of Electronic Packaging*, 139:011003–1–10, 2017.

[18] Thamer Khalif Salem Mete Budakli. Effect of polymer coating on vapor condensation heat transfer. *Journal of Heat Transfer*, 142, 2020.

[19] George Meyer. What's the Difference Between Heat Pipes and Vapor Chambers?, 2017.

[20] MOHAMED MOHAMED, KATERINA RALEVA, UMBERTO RAVAIOLI, DRAGICA VASILESKA, AND ZLATAN AKSAMIJA. Phonon dissipation in nanostructured semiconductor devices: Dispersing heat is critical for continued integrated circuit progress. *IEEE Nanotechnology Magazine*, 13(4):6,19, 2019 Aug.

[21] Mohammad Reza Shaeri, Daniel Attinger, Richard W. Bonner III . Vapor chambers with hydrophobic and biphilic evaporators in moderate to high heat flux applications. *Applied Thermal Engineering*, 130:83,92, 2018.

[22] Mohammad Shaeri. Dnaiel Attinger et al. Vapor chambers with hydrophobic and biliphilic evaporators in moderate to high heat flux applications. *Applied Thermal Engineering*, 130:83,92, 2018.

[23] Mohammad Shahed Ahamed, Yuji Saito, Koichi Mashiko, Masataka Mochizuki. Characterization of a high performance ultra-thin heat pipe cooling module for mobile hand held electronic devices. *Heat Mass Transfer*, 53:3241–3247, 2017.

[24] N. ZHU, K. VAFAItI . Analytical modeling of the startup characteristics of asymmetrical flat-plate and diskshaped heat pipes. *International Journal of Heat and Mass Transfer*, 17:2619,2637, 1998.

[25] R. Singh, A. Akbarzadeh, M. Mochizuki,. Effect of wick characteristics on the thermal performance of the miniature loop heat pipes,. *ASME. J. Heat Transfer*, 131:082601,1–10, 2009,Aug.

[26] Ram Ranjan, Jayathi Y.Murthy, Suresh V.Garimella, Unnikrishnan Vadakkan. A numerical model for transport in flat heat pipes considering wick microstructure effects. *International Journal of Heat and Mass Transfer*, 54:153,168, 2011.

[27] Rongfu Wena, Qian Lia, Wei Wanga, Benoit Latour, Calvin H. Li, Chen Li, Yung-Cheng Lee, Ronggui Yang. Enhanced bubble nucleation and liquid rewetting for highly efficient boiling heat transfer on two-level hierarchical surfaces with patterned copper nanowire arrays. *Nano Energy*, 38:59,65, 2017.

[28] Karl Rupp. 42 Years of Microprocessor Trend Data, 2018.

[29] Shanshan Xu Ryan Lewis. Thin flexible thermal ground planes: Fabrication and scaling characterization. *Journal of Microelectromechanical system*, 24:2040–2048, 2015 Dec.

[30] Ya-Ru Yang Shou-Shing Hsieh. Design, fabrication and performance tests for a polymer-based flexibleflat heat pipe. *Energy Conversion and Mana gemen*, 70:10–19, 2013.

[31] Kuo-Chun Hsieh Shwin-Chung Wong. A novel vapor chamber and its performance. *Internaltional Journal of Heat and Mass Transfer*, 53:2377–2384, 2010.

[32] Sooyoung Park Chunjong Park Soowon Kang, Hyeonwoo Choi. Fire in Your Hands: Understanding Thermal Behavior of Smartphones, 2019.

[33] Advanced Cooling Technologies. Vapor Chamber. `https://www.1-act.com/resources/heat-pipe-fundamentals/different-types-of-heat-pipes/vapor-chambers/`.

[34] Tingting Hao, Hongbin Ma, Xuehu Ma. Heat transfer performance of polytetrafluoroethylene oscillating heatpipe with water, ethanol, and acetone as working fluids. *International Journal of Heat and Mass Transfer*, 131:109,120, 2019.

[35] Unnikrishnan Vadakkan, Suresh V. Garimella,Jayathi Y. Murthy . Transport in flat heat pipes at high heat fluxes from multiple discrete sources. *Journal of Heat Transfer*, 126:347,354, 2004.

[36] Xianbing Ji. Jinliang Xu et al. Switchable heat transfer mechanisms of nucleation and convection by wettability matach of evaporator and condenser for heat pipes: Nanostrcutred surface effect. *Nano Energy*, 38:313,325, 2017.

[37] JinliangXu XianbingJi. Copper foam based vapor chamber for high heat flux dissipation. *Experimental Thermal and Fluid Science*, 40:93–102, 2012.

[38] Xiao Hou, Yapeng Chen, Wen Dai et al. Highly thermal conductive polymer composites via constructing micro-phragmites communis structured carbonfibers. *Chemical Engineering Journal*, 375:121921–1,121921–5, 2019.

[39] Yong Li, jiabin He, Hengfei He, Yuying Yan, Zhixin Zeng, Bo Li. Investigation of ultra-thin flattened heat pipes with sintered wick structure. *Applied Thermal Engineering*, 86:106–118, 2015.

[40] Yong Li, Wenjie Zhou, Zixi Li, Zhaoshu Chen, Yunhua Gan. Experimental analysis of thin vapor chamber with composite wick structure under different cooling conditions. *Applied Thermal Engineering*, 156:471–484, 2019.

[41] K. S. Yun Wang, Chen. *PEM fuel cells: thermal and water management fundamentals*. 2016.

[42] Yun Wang, Ken S.Chen. Advanced control of liquid water region in diffusion media of polymerelectrolyte fuel cells through a dimensionless number. *Journal of Power Sources*, 315:224,235, 2016.

[43] Yun Wang, Mehernosh Gundevia. Measurement of thermal conductivity and heat pipe effect in hydrophilic and hydrophobic carbon papers. *International Journal of Heat and Mass Transfer*, 60:134,142, 2013.

[44] Zezhou Zhu, Chaowei Li, Songfeng E et al. Enhanced thermal conductivity of polyurethane composites via engineeringsmall/large sizes interconnected boron nitride nanosheets. *Composites Science and Technology*, 170:93,100, 2019.